Optics Communications 559 (2024) 130444

Contents lists available at ScienceDirect

Optics Communications

journal homepage: www.elsevier.com/locate/optcom

Performance enhancement of RIS-assisted MRR-UOWC systems using the spectral-power-efficient LQAM-MPPM

Amr G. AbdElKader [a,b,*], Ahmed Allam [a], Kazutoshi Kato [c], Hossam M.H. Shalaby [b]

[a] Egypt-Japan University of Science and Technology (E-JUST), Alexandria 21934, Egypt
[b] Faculty of Engineering, Alexandria University, Alexandria 21544, Egypt
[c] Graduate School of Information Science and Electrical Engineering, Kyushu University, Fukuoka 819-0395, Japan

ARTICLE INFO

Keywords:
Optical wireless communication
Reconfigurable Intelligent Surface (RIS)
modulating retroreflector (MRR)
L-ary Quadrature Amplitude Modulation
Multi-Pulse Pulse-Position Modulation
(LQAM-MPPM) technique
Meijer s G-function
Fox H-function

ABSTRACT

Reconfigurable Intelligent Surfaces (RISs), proposed as innovative units, possess the potential to establish reliable connections in Underwater Optical Wireless Communication (UOWC) systems, where direct transmission (DT) experiences significant weakening due to dynamic channel conditions. In this paper, we examine the performance of a UOWC system consisting of an RIS and a modulating retroreflector (MRR), referred to as the RIS-assisted MRR-UOWC system. The channel is affected by a combination of path loss, gamma–gamma (G–G) turbulence, and pointing error (PE). The considered system employs the spectral-power-efficient L-ary Quadrature Amplitude Modulation Multi-Pulse Pulse-Position Modulation (LQAM-MPPM) technique. For our system performance measures, we present upper-bound (UB) and approximate UB expressions for the average bit-error rate (BER) of LQAM-MPPM signals. These expressions are used to analyze the system's performance. Performance metrics are established by deriving the Probability Density Function (PDF), Cumulative Distribution Function (CDF), and Moment-Generating Function (MGF) for the end-to-end signal-to-noise ratio (SNR), resulting from the sum of products of independent but not identically distributed (i.ni.d) channel coefficients. The results of our study indicate that the LQAM-MPPM scheme surpasses traditional schemes.

1. Introduction

The advancement of UOWC technology has opened avenues for high-data-rate systems in ocean exploration. These systems are characterized by elevated security levels and the absence of licensing requirements for wireless data transfers [1]. Given the constraints of limited bandwidth in radio frequency (RF) and acoustic technologies, coupled with a growing need for rapid underwater data transmission, UOWC has emerged as a practical and attractive solution [2].

Due to the absence of a direct link and the presence of barriers that create dead zones in wireless communication, installing UOWC is impractical for numerous applications. Cooperative relaying has been extensively studied to mitigate the impact of channel limitations and improve UOWC system performance [3]. RISs offer a promising and efficient alternative to active relaying methods, enhancing UOWC system performance without requiring complex processing at the relay. The RIS module consists of planar meta-surfaces used to direct the incoming signal towards a desired direction and adjust the transmission channel [4]. RISs employ a multitude of passive, cost-effective reflecting components in conjunction with integrated electronics to control the amplitude, phase, and polarization of incident signals, thereby improving signal quality and transmission coverage.

In conventional UOWC setups, two identical transceivers function as connecting terminals for data transmission within an unguided water environment. These transceivers utilize a narrow laser beam as the wireless optical carrier, providing several advantages, such as reduced power consumption and enhanced anti-interception capabilities. However, this choice necessitates the implementation of complex Pointing, Acquisition, and Tracking (PAT) systems in both transceivers [5]. As PAT systems typically consume a significant portion of power, mass, and dimensions in transceivers, conventional UOWC systems face limitations in deployment within harsh environments or on platforms with restricted capacity.

A noteworthy alternative involves constructing an asymmetrical UOWC system by replacing one transceiver with an MRR terminal comprising an MRR device and a photodetector. The MRR is typically constructed using a light modulator and a passive retroreflector [6]. Various methods, such as multiple quantum wells, micro-electromechanical

* Corresponding author at: Faculty of Engineering, Alexandria University, Alexandria 21544, Egypt.
E-mail addresses: amr.abdelkader@alexu.edu.eg (A.G. AbdElKader), ahmed.allam@ejust.edu.eg (A. Allam), kato@ed.kyushu-u.ac.jp (K. Kato), shalaby@ieee.org (H.M.H. Shalaby).

https://doi.org/10.1016/j.optcom.2024.130444
Received 10 December 2023; Received in revised form 29 February 2024; Accepted 3 March 2024
Available online 5 March 2024

systems, ferroelectric piezoelectric lead zirconate titanate thin films, and liquid crystals, have been employed to develop light modulators. The corner cube reflector and cat's eye reflector are commonly used retroreflectors [7]. Due to its low-power modulators and compact retroreflectors, the MRR can operate efficiently in diverse applications, such as communication with unmanned underwater vehicles (UUVs).

Hence, to leverage the advantages offered by both the RIS module and the MRR terminal, our focus will be on investigating the system known as the RIS-assisted MRR-UOWC system.

1.1. Related works

Several research investigations have been published exploring the advantages of the RIS technique across various wireless communication systems, encompassing both RF [8] and free-space optics (FSO) [9]. A comprehensive investigation into the performance of RIS-assisted wireless communication under general Fox H fading channels has been presented in [10]. Efforts to integrate an FSO connection over gamma–gamma (G–G) turbulence and pointing error (PE) with an RIS-assisted RF link over Rayleigh fading were explored in [11] through decode-and-forward relaying.

Recent proposals have also considered leveraging RIS for connected autonomous vehicles and vehicular networks [12,13], taking into account the benefits of traditional wireless communications. In [13], the authors investigated the average BER, outage probability, and ergodic capacity of a mobile network enabled with RIS and subject to random user movement. The effectiveness of multiple RIS-based vehicle communications was explored using a double Generalized-Gamma fading model in [14].

Numerous research studies have been published, focusing on the advancement of MRR devices [15,16], along with the practical implementations of MRR FSO networks [17,18]. These works collectively underscore the viability of MRR FSO technology.

Following the introduction of QAM-MPPM in [19,20] examined the maximum power efficiencies of LQAM-MPPM under spectral efficiency restrictions, and LQAM-MPPM was shown to be the most power-efficient scheme. The performance enhancement of DT MRR-UOWC system using LQAM-MPPM was investigated in [21].

1.2. Motivations

As far as we know, there is no prior research proposing the use of the LQAM-MPPM technique in a RIS-assisted MRR-UOWC system employing intensity modulation/direct detection (IM/DD) and featuring a channel characterized by path loss, G–G turbulence, and PE. This focus constitutes the primary emphasis of the present manuscript. The main goals of this investigation include deriving both UB and approximate UB expressions for the average BER of LQAM-MPPM signals. Subsequently, these expressions are applied to evaluate the performance of the RIS-assisted MRR-UOWC system under investigation.

1.3. Contributions

The main contributions in this paper are:

1. Deriving the PDF of the combined statistical impact of path loss with G–G turbulence and PE in an RIS-assisted MRR-UOWC system, expressed in terms of the multivariate Fox H function (MFHF). This is achieved by considering the sum of products of i.ni.d fading coefficients.
2. Utilizing this result, we develop analytical expressions in closed form for the PDF, and CDF of the instantaneous electrical SNR γ_{RIS} for the RIS-assisted MRR-UOWC system.
3. Using the obtained PDF and CDF of γ_{RIS}, we assess the performance of the examined system by formulating an UB closed-form expression for the average BER of LQAM-MPPM signals in terms of MFHF.

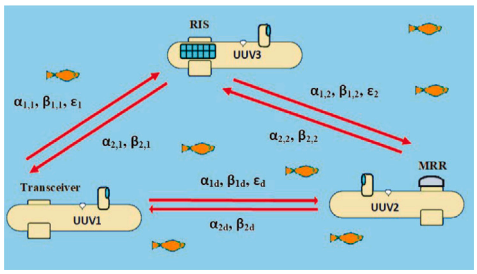

Fig. 1. System model.

4. By employing the Gauss–Laguerre quadrature rule (GLQR), we develop an approximate UB closed-form expression for the average BER of LQAM-MPPM signals.
5. Providing numerical results for both the UB and approximate UB closed-form expressions. The results exhibit substantial agreement between the two expressions, highlighting the efficacy of the hybrid modulation technique compared to conventional methods, namely LQAM and MPPM, in both clear ocean and coastal ocean environments.

1.4. Paper organization

The next sections of this paper are organized as follows: Section 2 provides a comprehensive explanation of the system and channel models. Section 3 contains the statistical analysis of RIS-assisted MRR-UOWC system. Section 4 presents the performance analysis, which includes UB and approximate UB closed-form expressions for the average BER of LQAM-MPPM signals. In Section 5, the discussion of numerical results is presented. Finally, the conclusions are summarized in Section 6.

2. System and channel models

In this section, we consider a scenario that illustrates the RIS-assisted MRR-UOWC system model. Additionally, we provide a detailed description of the basic schematic block diagrams for both the transmitter and receiver in the transceiver of the LQAM-MPPM technique. Finally, we present the mathematical equations that represent the fading in the channel.

2.1. System model

Let us consider a scenario in which an UUV named UUV1, equipped with a transceiver, establishes communication with another UUV named UUV2, which is equipped with an MRR unit, as illustrated in Fig. 1. In cases where a direct link between the transceiver and the MRR unit is unavailable, an N-element RIS module, positioned on the body of a third UUV named UUV3, is interposed between the transceiver and the MRR unit. This module is employed to establish a line-of-sight connection between the RIS and both the transceiver and the MRR unit. Consequently, the RIS module reflects the incident signal to direct the transmitted light towards the MRR unit. Upon reaching the MRR unit, the transmitted light undergoes information encoding and is then conveyed back towards the RIS module, which reflects it back towards the transceiver. The signal containing the information is subsequently extracted at the transceiver.

We assume precise knowledge of the channel phase at each element of the RIS. Additionally, we consider the elements of the RIS to be separated by half a wavelength, implying that the distance between the elements on the RIS should be on the order of nanometers. Although optical meta-surfaces share conceptual similarities with RF meta-surfaces, the nanoscale technologies enabling their realization

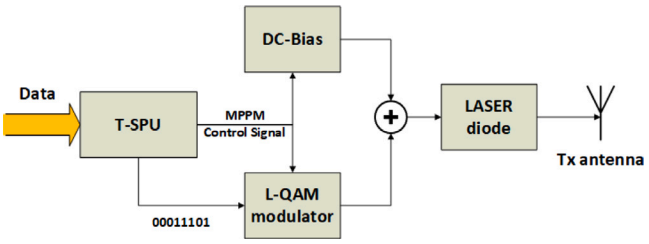

Fig. 2. Block diagram of a hybrid LQAM-MPPM transmitter.

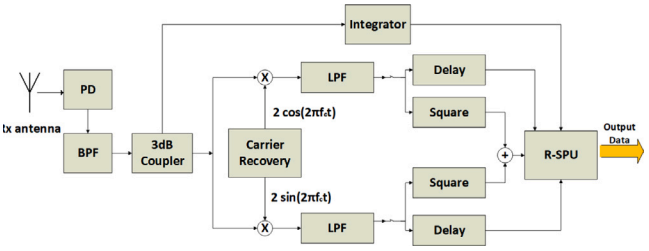

Fig. 3. Block diagram of a hybrid LQAM-MPPM receiver.

at optical frequencies differ significantly from the standard antenna technologies used in RF bands. In [9], the authors conducted a review of reconfigurable meta-surfaces, including various implementation examples. The majority of reconfigurable meta-surfaces utilize materials with optical properties that can be modified by external electrical, mechanical, thermal, or optical stimuli. The review emphasizes two key mechanisms that facilitate the tunability of optical meta-surfaces: field-effect tuning and structural change-induced tuning.

2.2. LQAM-MPPM transceiver setup

In the MPPM technique, the symbol duration T is divided into K time slots, each lasting T_s, with optical power present in w time slots only. LQAM signals are utilized in the hybrid LQAM-MPPM scheme to modulate the optical pulses within the MPPM frame. The data rate for systems employing this hybrid technique is expressed as [20]:

$$R_b = \frac{\lfloor \log_2 \binom{K}{w} \rfloor + wm}{KT_s} \tag{1}$$

Here, $m = \log_2 L$ represents the number of bits per LQAM symbol, and L denotes the cardinality of the LQAM constellation. $\binom{K}{w}$ signifies the cardinality of the MPPM constellation, and $\lfloor \log_2 \binom{K}{w} \rfloor$ represents the floor integer of the number of bits per MPPM symbol, i.e., the maximum integer less than $\binom{K}{w}$. Considering the utilization of LQAM-MPPM in the study, Fig. 2 illustrates the fundamental configuration of the transmitter, while Fig. 3 depicts that of the receiver for this hybrid scheme.

At the transmitter side, a frame composed of $\lfloor \log_2 \binom{K}{w} \rfloor + wm$ bits is fed into the transmitter signal-processing unit (T-SPU). The T-SPU manipulates these bits to regulate the operation of both LQAM and the DC-Bias level. Utilizing $\lfloor \log_2 \binom{K}{w} \rfloor$ bits (MPPM data-word part), the T-SPU determines the positions of w signal-slots within a frame of K time-slots. This control signal governs the activation and deactivation of both the DC-Bias and the LQAM modulator. Through this data manipulation, a control signal is generated, enabling the decoding of wm bits (LQAM data-word part) during the w signal time-slots. The resulting output from the LQAM modulator is then combined with the output from the DC-biasing source, thereby illuminating the laser diode.

For a signal time slot, and for $0 \le t < T_s$, the laser's output optical power is directly proportional to the modulating LQAM signals, as follows [19]:

$$\mathrm{P(t)} = \frac{KP_s}{w} \sum_{u=0}^{K-1} \left[1 + M\{A_I \cos(2\pi f_c t) - A_Q \sin(2\pi f_c t)\} \right] \times \mathrm{rect}\left(t - uT_s\right) \tag{2}$$

where P_s is the average optical power of the transmitted signal that is normalized to unit amplitude, M is the modulation index, A_I and A_Q being the signal amplitudes of in-phase and quadrature components, respectively, and f_c is the electrical carrier frequency.

On the receiving end, the photodiode (PD) transforms the received optical intensity variations into corresponding electrical domain variations. The output current of the PD is expressed as:

$$y(t) = I_{\mathrm{ph}} \sum_{u=0}^{K-1} [1 + M\{A_I \cos(2\pi f_c t) - A_Q \sin(2\pi f_c t)\}] \times \mathrm{rect}\left(t - uT_s\right) + n(t), \tag{3}$$

with

$$I_{\mathrm{ph}} = R\frac{KP_s}{w} \left(\frac{\eta A}{\lambda \sum_{i=1}^{N} \sum_{j=1}^{2} z_{i,j}} \right)^2 H_{\mathrm{RIS}}, \tag{4}$$

where I_{ph} is the DC component of the received photocurrent $y(t)$, $n(t)$ is Additive White Gaussian Noise (AWGN) with a mean of zero and a variance of σ_n^2, R is the responsivity of the PD, η is the efficiency of both the transmitter and receiver optics inside the transceiver, A is the transceiver telescopic area, λ is the optical wavelength, $i \in \{1, 2, \ldots, N\}$ represents the number of the RIS elements, $j \in \{1, 2\}$ represents the path number (i.e., $j = 1$ represents the path between the transceiver and the ith RIS element, whereas $j = 2$ represents the path between the ith RIS element and the MRR unit), $z_{i,1}$ is the distance between the transceiver and the RIS, and $z_{i,2}$ is the distance between the RIS and MRR unit. H_{RIS} represents the channel fading arising from the combined impact of G–G turbulence, and PE with the path loss in case of RIS-assisted MRR-UOWC link. On the other hand, for a non-signal time slot, $P(t) = 0$, and hence, $y(t) = n(t)$.

The resulting signal undergoes band-limiting through a band-pass filter (BPF) to cancel out-of-band noise and distortion, thereby enhancing the quality of the received signal. Subsequently, a 3 dB coupler directs the band-limited signal into two arms.

In the upper arm (MPPM demodulator), the signal undergoes integration over each time slot, T_s, and is then forwarded to the receiver signal-processing unit (R-SPU). Within the R-SPU, the integrated signal is digitized using an analog-to-digital converter and stored. The K stored levels are organized in descending order to identify the w highest levels, corresponding to the signal time-slots of the MPPM symbol. Following this, the R-SPU decodes MPPM symbols based on the MPPM symbols-to-bits map.

On the other arm (LQAM demodulator), the decoding of LQAM data occurs after a fixed delay-line of two-frames duration. This delay provides sufficient time for the R-SPU to determine the position of the w highest level time-slots. These w time-slots encompass the w LQAM symbols. Mixers equipped with low-pass filters (LPFs) extract the in-phase and quadrature-phase signal components. Subsequently, the positions of the w highest-level time-slots dictate the anticipated time-slots for identifying LQAM symbols. Following this, the R-SPU decodes the selected LQAM symbols based on the LQAM symbols-to-bits map. Ultimately, the received data words are reconstructed from the decoded MPPM and LQAM bits.

Now, when considering the decision metric for decoding, it is important to note that LQAM-MPPM combines two modulation schemes: LQAM for amplitude and phase modulation, and MPPM for pulse position modulation. Consequently, the decision metric incorporates both the amplitude and the position of the received pulses.

The decision metric for decoding LQAM-MPPM can be expressed as a combination of the decision metrics for LQAM and MPPM. Thus, for LQAM-MPPM, the decision metric (d_{hybrid}) for each symbol is calculated as follows:

$$d_{\text{hybrid}} = d_{L\text{QAM}} + d_{\text{MPPM}} \tag{5}$$

Here, $d_{L\text{QAM}}$L represents the decision metric for LQAM, calculated as the Euclidean distance within the LQAM constellation, considering both the received amplitude and phase information. Similarly, d_{MPPM} stands for the decision metric for MPPM, determined as the difference in pulse positions between the received position and the expected positions, considering the received pulse position information. Assuming an MPPM system with n possible positions, each represented as a point in an n-dimensional space, d_{MPPM} between the received position, P_i, and the expected position, P_j, can be calculated using the formula: $d_{\text{MPPM}} = \sqrt{\sum_{a=1}^{n}(P_{i,a} - P_{j,a})^2}$. Here, $P_{i,a}$ and $P_{j,a}$ represent the ath component (dimension) of the positions P_i and P_j. The summation is performed over all dimensions, and the square root of the sum provides the distance between the two positions.

The decision rule involves selecting the combination of LQAM level and MPPM pulse position that minimizes the overall decision metric. The specific expressions for $d_{L\text{QAM}}$L and d_{MPPM} will vary based on the modulation scheme's details, such as the LQAM constellation diagram, the number of pulses in MPPM, and the characteristics of the channel.

The SNR of the received LQAM symbol is

$$\text{SNR} = \frac{P_{L\text{QAM}}}{\sigma_n^2}, \tag{6}$$

where $P_{L\text{QAM}}$L is the LQAM symbol desired signal power given by

$$P_{L\text{QAM}} = \frac{1}{2} M^2 I_{\text{ph}}^2, \tag{7}$$

and the noise variance is given by

$$\sigma_n^2 = \frac{1}{T_s}\left[\frac{4K_b T_{\text{abs}} F}{R_L} + \frac{2qwI_{\text{ph}}}{K} + \frac{w^2 I_{\text{ph}}^2}{K^2}\text{RIN}\right], \tag{8}$$

where RIN is the relative intensity noise, K_b is Boltzmann's constant, T_{abs} is absolute temperature, F is the noise figure of receiver electronics, R_L is the PD load resistor, and q is the electron charge.

As indicated in Eq. (8), it is essential to recognize that assuming AWGN does not automatically imply negligible signal-dependent noise. Signal-dependent noise fluctuates based on signal characteristics. While the AWGN model assumes independence between noise and signal, it does not explicitly rule out the possibility of signal-dependent noise.

In this context, RIN is not a random noise form like AWGN; rather, it signifies fluctuations in the optical power of the laser over time. Characterized by the ratio of power fluctuations at a specific frequency to the average power of the signal (measured in dB/Hz), these variations in laser output power are influenced by factors such as spontaneous emission processes within the laser medium, inherently tied to the optical signal itself. Consequently, RIN is considered a type of signal-dependent noise, impacting the intensity of the optical signal, leading to signal degradation, and influencing the overall performance of our system.

2.3. Channel model

We consider the elements of the RIS to be separated by half a wavelength, assuming i.ni.d channels at the RIS [22]. The channels between the transceiver and the RIS, and between the RIS and the MRR, are generally considered independent distributed channels. The independence arises from the ability to treat these channels separately. In systems with an RIS, both channels are typically viewed as independent due to the RIS acting as a passive reflecting surface, enabling independent optimization without direct interaction between channels. Despite their independence, the intelligent reconfiguration of the RIS can optimize signal propagation for both channels, influencing overall system efficiency. Both channels are not necessarily identical. This is achieved by considering different values for the parameters of channel fading from the transceiver to the RIS and from the RIS to the MRR unit. These variations necessitate the independent consideration of each channel for system analysis and optimization. In practice, while treated as independent for analysis, the actual characteristics of both channels can exhibit variations, rendering them non-identically distributed.

On the other hand, regarding the channel between the transceiver and the RIS unit (or between the RIS unit and the MRR unit), with a beam radius significantly larger than the nanometer scale of the RIS elements, the optical spot effectively spans the entire RIS, engaging with nanoscale elements concurrently. This implies that the same optical beam interacts simultaneously with all RIS elements. When the nanometer scale RIS elements are closely spaced and the optical beam interacts with them simultaneously, it can induce spatial correlation among the channels. In this context, spatial correlation implies that changes in channel conditions affecting one element may similarly impact others, resulting in dependent channels. Additionally, if the RIS is configured to coherently manipulate the optical beam across its entire surface, it may introduce correlation among the channels.

When the receiver aperture exceeds the size of the RIS elements, the dependence of channels can be influenced by various conditions. Critical factors encompass spatial correlation, RIS design, common environmental influences, limited angular separation, and strong crosstalk effects. Spatial correlation emerges when nanoscale RIS elements are closely positioned, potentially leading to channel dependence as the larger receiver aperture captures signals from nearby elements. Coherent manipulation of the optical beam across the entire RIS surface introduces correlation among channels, resulting in dependency if the designed RIS manipulates the optical beam coherently. Common environmental influences can also contribute to channel dependence, as the larger aperture captures shared factors such as water conditions. Limited angular separation between channels with distinct optical characteristics may lead to dependence, as the larger aperture captures signals from closely aligned channels. Additionally, crosstalk can contribute to channel dependence if significant effects occur among neighboring nanoscale elements, captured by the larger receiver aperture.

The channel fading arising from the combined impact of G–G turbulence, and PE with the path loss in case of RIS-assisted MRR-UOWC link, is given as

$$H_{RIS} = h_{lRIS} h_{fRIS} h_{bRIS} \tag{9}$$

where h_{lRIS} is the path loss of the RIS-assisted MRR-UOWC link, which is given as

$$h_{lRIS} = \exp\left[-2c(\lambda)\sum_{i=1}^{N}\sum_{j=1}^{2} z_{i,j}\right] \tag{10}$$

where $c(\lambda)$ is the attenuation coefficient. To reduce the complexity of calculations, we assume $z_{1,1} = z_{2,1} = \ldots = z_{N,1} = z_1$ and $z_{1,2} = z_{2,2} = \ldots = z_{N,2} = z_2$. The flat fading coefficients for the RIS-assisted MRR-UOWC link between transceiver and MRR unit for the forward path and the backward path, respectively are given as:

$$h_{fRIS} = \sum_{i=1}^{N}\prod_{j=1}^{2} h_{f_{i,j}} \tag{11}$$

and

$$h_{bRIS} = \sum_{i=1}^{N}\prod_{j=1}^{2} h_{bi,j} \tag{12}$$

where $h_{f_{i,j}}$ and $h_{bi,j}$ are the forward and backward channel fading coefficients for the ith RIS element in the jth path, respectively.

G–G turbulence and PE are the two main signal degradation factors that affect the RIS-assisted connection in addition to the path loss. The

PDF of the G–G distribution, $f_{h_t}(h_t)$, is [23]:

$$f_{h_t}(h_t) = \frac{2(\alpha\beta)^{\frac{\alpha+\beta}{2}}}{\Gamma(\alpha)\Gamma(\beta)} h_t^{\frac{\alpha+\beta}{2}-1} \times K_{\alpha-\beta}\left(2\sqrt{\alpha\beta h_t}\right), \qquad h_t > 0 \tag{13}$$

where h_t represents the channel fading coefficient due to G–G turbulence, $\Gamma(\cdot)$ is the gamma function, $K_x(\cdot)$ is the modified Bessel function of the second kind of order x. The terms α and β denote the effective numbers of small-scale and large-scale eddies within the scattering environment, and these parameters are correlated with the turbulence circumstances. Assuming plane wave propagation, the parameters α and β can be defined as follows [24]:

$$\alpha = \left[\exp\left(\frac{0.49{\sigma_l}^2}{(1+1.11{\sigma_l}^{12/5})^{7/6}}\right) - 1\right]^{-1} \tag{14}$$

and

$$\beta = \left[\exp\left(\frac{0.51{\sigma_l}^2}{(1+0.69{\sigma_l}^{12/5})^{5/6}}\right) - 1\right]^{-1} \tag{15}$$

where ${\sigma_l}^2$ is the Rytov scintillation index of the plane wave given as in [24]. The PDF of the zero-boresight PE, $f_p(h_p)$, is [25]:

$$f_{hp}(h_p) = \frac{\epsilon^2}{A_o^{\epsilon^2}} h_p^{\epsilon^2-1}, \quad 0 \le h_p \le A_o \tag{16}$$

where h_p represents the channel fading coefficient attributed to the PE, A_o denotes the PE fading coefficient under zero PE conditions, and ϵ is the ratio between the equivalent beam radius at the destination and the PE displacement standard deviation (SD) at this destination. Although analyzing the considered system with generalized PE would be interesting, we use the zero-boresight model (as used in many references) to avoid complicated analytical formulas. Furthermore, nonzero boresight and unequal jitter have no effect on the performance of the systems [26].

3. Closed-form statistical analysis

In this section, we derive the closed-form formulas for the PDF, and CDF of γ_{RIS} as follows:

1. By employing the Mellin transform (MT), we determine the PDF for the product of two i.ni.d random variables (RVs) associated with the forward path $h_{fi} = \prod_{j=1}^{2} h_{fi,j}$ and the backward path $h_{bi} = \prod_{j=1}^{2} h_{bi,j}$.
2. For N-RIS elements, we develop statistical results of the PDFs of h_{fRIS}, and h_{bRIS}.
3. We derive the PDF of H_{RIS}, and hence, using RV transformation, obtain the PDF and CDF of $\gamma_{RIS} = (K/w)^2 H_{RIS}^2 \overline{\gamma}_{RIS}$, where $\overline{\gamma}_{RIS}$ is the average SNR of the RIS-assisted MRR-UOWC system.

Although we can model the channel coefficients $h_{fi,1}$ and $h_{fi,2}$ to be similar, we make a general assumption that the fading coefficients $h_{fi,1}$ and $h_{fi,2}$ are i.ni.d. Similarly, we assume that $h_{bi,1}$ and $h_{bi,2}$ are i.ni.d. Hence, we express $h_{fi,1} = h_{t1}h_{p1}$, $h_{fi,2} = h_{t2}h_{p2}$, $h_{bi,1} = h_{t1}$, and $h_{bi,2} = h_{t2}$. Here, $h_{fi,1}$ is the channel fading coefficient of the forward path between the transceiver and the ith element of the RIS module. $h_{fi,2}$ is the channel fading coefficient of the forward path between the ith element of the RIS module and the MRR unit. $h_{bi,1}$ is the channel fading coefficient of the backward path between the transceiver and the ith element of the RIS module, and $h_{bi,2}$ is the channel fading coefficient of the backward path between the ith element of the RIS module and the MRR unit. Furthermore, h_{t1} and h_{t2} are the G–G turbulence channel fading coefficients between the transceiver and the ith element of the RIS module and between the ith element of the RIS module and the MRR unit, respectively. Additionally, h_{p1} and h_{p2} represent the channel fading coefficients caused by the PE in the forward path from the transceiver to the ith element of the RIS module and from the ith element of the RIS module to the MRR unit, respectively.

For the forward path, we apply the MT to obtain the PDF of $h_{fi} = \prod_{j=1}^{2} h_{fi,j} = h_{fi,1}h_{fi,2}$. Here, $h_{fi,1}$ and $h_{fi,2}$ are considered to be i.ni.d RVs distributed according to Eq. (13). Thus, the PDF of h_{fi} is given as:

$$f_{h_{fi}}(x) = \frac{1}{2\pi j}\frac{1}{x}\int_{\mathcal{L}} \mathbb{E}[h_{fi}^r] x^{-r} dr \tag{17}$$

where

$$\mathbb{E}[h_{fi}^r] = \prod_{j=1}^{2} \mathbb{E}[h_{fi,j}^r] = \prod_{j=1}^{2} \int_0^\infty u^r f_{h_{fi,j}}(u)\, du \tag{18}$$

This is the rth moment of h_{fi}. Here, in the complex r-plane, $\mathcal{L}$ is an infinite contour with no singularities in the integrand in Eq. (17). In a manner similar to that used to derive ([21],Eq.(7)), $f_{h_{fi,j}}(x)$ is derived. The resulted expression is then substituted in Eq. (18) and using the identity ([27], Eq.(07.34.21.0009.01)) to get the rth moment of h_{fi} as

$$\mathbb{E}[h_{fi}^r] = \prod_{j=1}^{2} \left\{ \frac{\nu_{fj}}{{\rho_{fj}}^r} \times \frac{\Gamma(r+{\epsilon_j}^2)\Gamma(r+\alpha_{1,j})\Gamma(r+\beta_{1,j})}{\Gamma(r+{\epsilon_j}^2+1)} \right\} \tag{19}$$

where $\nu_{fj} = {\epsilon_j}^2/\left(\Gamma(\alpha_{1,j})\Gamma(\beta_{1,j})\right)$, and $\rho_{fj} = (\alpha_{1,j}\beta_{1,j})/A_o$. $\alpha_{1,1}$ and $\beta_{1,1}$ denote the large-scale and small-scale parameters of the forward path between the transceiver and the RIS module, respectively. Similarly, $\alpha_{1,2}$ and $\beta_{1,2}$ represent the large-scale and small-scale parameters of the forward path between the RIS module and the MRR unit, respectively. Furthermore, ϵ_1 is the ratio between the equivalent beam radius at the RIS module and the PE displacement SD at that module when light travels from the transceiver to the RIS module. Similarly, ϵ_2 is the ratio between the equivalent beam radius at the MRR unit and the PE displacement SD at the MRR when light travels from the RIS module to the MRR unit. Substituting Eq. (19) into Eq. (17) and employing the Meijer's G-function (GF) definition ([27], Eq.(07.34.02.0001.01)), we obtain the PDF of h_{fi} as:

$$f_{h_{fi}}(x) = \frac{\prod_{j=1}^{2}\nu_{fj}}{x} \times G_{2,6}^{6,0}\left(x\prod_{j=1}^{2}\rho_{fj}\middle|\begin{matrix}\{{\epsilon_j}^2+1\}_{j=1}^2 \\ \{{\epsilon_j}^2,\alpha_{1,j},\beta_{1,j}\}_{j=1}^2\end{matrix}\right) \tag{20}$$

For the backward path, to derive the PDF of h_{bi}, we use a similar approach to the one employed in deriving $f_{h_{bi}}(x)$. In this process, we derive the rth moment of h_{bi} as follows:

$$\mathbb{E}[h_{bi}^r] = \prod_{j=1}^{2}\left\{ \frac{\nu_{bj}}{{\rho_{bj}}^r} \times \Gamma(r+\alpha_{2,j})\Gamma(r+\beta_{2,j}) \right\} \tag{21}$$

where $\nu_{bj} = 1/\Gamma(\alpha_{2,j})\Gamma(\beta_{2,j})$, and $\rho_{bj} = \alpha_{2,j}\beta_{2,j}$. The parameters $\alpha_{2,2}$ and $\beta_{2,2}$ correspond to the large-scale and small-scale parameters, respectively, of the backward path between the MRR unit and the RIS module. Similarly, $\alpha_{2,1}$ and $\beta_{2,1}$ represent the large-scale and small-scale parameters, respectively, of the backward path between the RIS module and the transceiver. Substituting Eq. (21) into Eq. (17) and employing the GF definition ([27], Eq.(07.34.02.0001.01)), we obtain the PDF of h_{bi} as:

$$f_{h_{bi}}(x) = \frac{\prod_{j=1}^{2}\nu_{bj}}{x} \times G_{0,4}^{4,0}\left(x\prod_{j=1}^{2}\rho_{bj}\middle|\begin{matrix}- \\ \{\alpha_{2,j},\beta_{2,j}\}_{j=1}^2\end{matrix}\right) \tag{22}$$

For N RIS elements, to obtain the PDF of the forward path's channel fading $h_{fRIS} = \sum_{i=1}^{N} h_{fi}$, using ([28], Eq. (7)), the MGF of h_{fi} can be expressed as

$$\begin{aligned} M_{h_{fi}}(s) = \frac{1}{2\pi j}\prod_{j=1}^{2}\nu_{fj}{\rho_{fj}}^r \int_{\mathcal{L}}\left[\int_0^\infty e^{-sx}x^{r-1}dx\right] \\ \times\prod_{j=1}^{2}\frac{\Gamma(r+{\epsilon_j}^2)\Gamma(r+\alpha_{1,j})\Gamma(r+\beta_{1,j})}{\Gamma(r+{\epsilon_j}^2+1)}dr \end{aligned} \tag{23}$$

Solving the inner integral in Eq. (23) as

$$\int_0^\infty e^{-sx}x^{r-1}\,dx = s^{-r}\Gamma(r) \tag{24}$$

Substituting Eq. (24) into Eq. (23) and employing the GF definition ([27], Eq.(07.34.02.0001.01)), we get:

$$M_{h_{fi}}(s) = \prod_{j=1}^{2} \nu_{fj} \times G_{3,6}^{6,1}\left(\frac{1}{s} \prod_{j=1}^{2} \rho_{fj} \middle| \begin{matrix} \{\epsilon_j{}^2+1\}_{j=1}^2, 1 \\ \{\epsilon_j{}^2, \alpha_{1,j}, \beta_{1,j}\}_{j=1}^2 \end{matrix} \right) \tag{25}$$

By applying the inverse Laplace transform to the MGF, we obtain the PDF of h_{fRIS} as:

$$f_{h_{fRIS}}(x) = \mathscr{L}^{-1}\left\{ \prod_{i=1}^{N} M_{h_{fi}}(s) \right\} \tag{26}$$

Substituting Eq. (25) into Eq. (26) and reversing the integration order, we obtain:

$$\begin{aligned} f_{h_{fRIS}}(x) = & \prod_{i=1}^{N} \prod_{j=1}^{2} \nu_{fi,j} \times \left\{ \left(\frac{1}{2\pi j} \right)^N \int_{\mathcal{L}_i} \left(\prod_{j=1}^{2} \rho_{fi,j} \right)^{r_i} \right. \\ & \times \prod_{j=1}^{2} \frac{\Gamma(r_i + \epsilon_j{}^2)\Gamma(r_i + \alpha_{1,j})\Gamma(r_i + \beta_{1,j})}{\Gamma(r_i + \epsilon_j{}^2 + 1)} \\ & \left. \times \left[\frac{1}{2\pi j} \int_{\mathcal{L}} \exp(sx) \times s^{-\Sigma_{i=1}^{N} r_i} ds \right] dr_i \right\} \end{aligned} \tag{27}$$

where $\nu_{f1,1} = \nu_{f2,1} = \cdots = \nu_{fN,1}$, $\nu_{f1,2} = \nu_{f2,2} = \cdots = \nu_{fN,2}$, $\rho_{f1,1} = \rho_{f2,1} = \cdots = \rho_{fN,1}$, and $\rho_{f1,2} = \rho_{f2,2} = \cdots = \rho_{fN,2}$, serve to reduce the complexity of calculations. In the complex n_i-plane, $\mathcal{L}_i$ is an infinite contour with no singularities in the integrand in Eq. (27). The convergence conditions of multiple contour integrals describing MFHF are provided in [29]. Solving the inner integral in Eq. (27) as

$$\frac{1}{2\pi j} \int_{\mathcal{L}} \exp(sx) \times s^{-\Sigma_{i=1}^{N} r_i} ds = \frac{x^{-1+\Sigma_{i=1}^{N} r_i}}{\Gamma(\sum_{i=1}^{N} r_i)}, \tag{28}$$

Substituting Eq. (28) into Eq. (27) and employing the N-MFHF definition ([30], A.1), we obtain:

$$\begin{aligned} f_{h_{fRIS}}(x) = & \frac{\prod_{i=1}^{N} \prod_{j=1}^{2} \nu_{fi,j}}{x} \times H_{0,1:3,6;\ldots;3,6}^{0,0:6,1;\ldots;6,1} \\ & \left(\left\{ x \prod_{j=1}^{2} \rho_{fj} \right\}_1^N \middle| \begin{matrix} -:\left\{(1,1),\{(\epsilon_j{}^2+1,1)\}_{j=1}^2\right\}_1^N \\ (1;\{1\}_1^N):\left\{\{(\epsilon_j{}^2,1),(\alpha_{1,j},1),(\beta_{1,j},1)\}_{j=1}^2\right\}_1^N \end{matrix} \right) \end{aligned} \tag{29}$$

For the backward path, to derive the PDF of $h_{bRIS} = \sum_{i=1}^{N} h_{bi}$, we use a similar method as that employed for deriving h_{fRIS}, where

$$\begin{aligned} M_{h_{bi}}(s) = & \frac{1}{2\pi j} \prod_{j=1}^{2} \nu_{bj} \rho_{bj}{}^r \int_{\mathcal{L}} \left[\int_0^{\infty} e^{-sx} x^{r-1} dx \right] \\ & \times \prod_{j=1}^{2} \left\{ \Gamma(r + \alpha_{2,j})\Gamma(r + \beta_{2,j}) \right\} dr \end{aligned} \tag{30}$$

In Eq. (30), the inner integral is the same as the one solved in Eq. (24). By substituting Eq. (24) into Eq. (30) and using the GF definition ([27], eq.(07.34.02.0001.01)), we obtain:

$$M_{h_{bi}}(s) = \prod_{j=1}^{2} \nu_{bj} \times G_{1,4}^{4,1}\left(\frac{1}{s} \prod_{j=1}^{2} \rho_{bj} \middle| \begin{matrix} 1 \\ \{\alpha_{2,j}, \beta_{2,j}\}_{j=1}^2 \end{matrix} \right) \tag{31}$$

Substituting Eq. (31) into Eq. (26) and reversing the integration order, we obtain:

$$\begin{aligned} f_{h_{bRIS}}(x) = & \prod_{i=1}^{N} \prod_{j=1}^{2} \nu_{bi,j} \times \left\{ \left(\frac{1}{2\pi j} \right)^N \int_{\mathcal{L}_i} \left(\prod_{j=1}^{2} \rho_{bi,j} \right)^{r_i} \right. \\ & \times \prod_{j=1}^{2} [\Gamma(r_i + \alpha_{2,j})\Gamma(r_i + \beta_{2,j})] \\ & \left. \times \left[\frac{1}{2\pi j} \int_{\mathcal{L}} \exp(sx) \times s^{-\Sigma_{i=1}^{N} r_i} ds \right] dr_i \right\} \end{aligned} \tag{32}$$

where $\nu_{b1,1} = \nu_{b2,1} = \ldots = \nu_{bN,1}$, $\nu_{b1,2} = \nu_{b2,2} = \ldots = \nu_{bN,2}$, $\rho_{b1,1} = \rho_{b2,1} = \ldots = \rho_{bN,1}$ and $\rho_{b1,2} = \rho_{b2,2} = \ldots = \rho_{bN,2}$ for reducing the complexity of calculations. Substituting Eq. (28) into Eq. (32) and employing the N-MFHF definition ([30], A.1), we obtain:

$$\begin{aligned} f_{h_{bRIS}}(x) = & \frac{\prod_{i=1}^{N} \prod_{j=1}^{2} \nu_{bi,j}}{x} \times H_{0,1:1,4;\ldots;1,4}^{0,0:4,1;\ldots;4,1} \\ & \left(\left\{ x \prod_{j=1}^{2} \rho_{bj} \right\}_1^N \middle| \begin{matrix} -:\{(1,1)\}_1^N \\ (1;\{1\}_1^N):\left\{\{(\alpha_{2,j},1),(\beta_{2,j},1)\}_{j=1}^2\right\}_1^N \end{matrix} \right) \end{aligned} \tag{33}$$

Utilizing the derived PDFs for the forward and backward paths in Eqs. (29) and (33), the PDF of H_{RIS} is given as [31]:

$$f_{H_{RIS}}(H_{RIS}) = \int f_{H_{RIS}|h_{fRIS}}(H_{RIS}|h_{fRIS}) f_{h_{fRIS}}(h_{fRIS}) dh_{fRIS} \tag{34}$$

where $f_{H_{RIS}|h_{fRIS}}(H_{RIS}|h_{fRIS})$ is the conditional probability given $h_{f,RIS}$, which is derived to be:

$$\begin{aligned} f_{H_{RIS}|h_{fRIS}}(H_{RIS}|h_{fRIS}) = & \prod_{i=1}^{N} \prod_{j=1}^{2} \nu_{bi,j} \times H_{0,1:1,4;\ldots;1,4}^{0,0:4,1;\ldots;4,1} \\ & \left(\left\{ \frac{H_{RIS}}{h_{fRIS}} \prod_{j=1}^{2} \rho_{bj} \right\}_1^N \middle| \begin{matrix} -:\{(1,1)\}_1^N \\ (1;\{1\}_1^N):\left\{\{(\alpha_{2,j},1),(\beta_{2,j},1)\}_{j=1}^2\right\}_1^N \end{matrix} \right) \end{aligned} \tag{35}$$

Substituting Eqs. (29) and (35) in Eq. (34) leads to:

$$\begin{aligned} f_{H_{RIS}}(H_{RIS}) = & \frac{\prod_{i=1}^{N} \prod_{j=1}^{2} \nu_{ri,j}}{H_{RIS}} \times H_{0,2:4,10;\ldots;4,10}^{0,0:10,2;\ldots;10,2} \\ & \left(\left\{ \frac{H_{RIS}}{h_{lRIS}} \prod_{j=1}^{2} \rho_j \right\}_1^N \middle| \begin{matrix} -:\left\{(1,1),(1,1),\{(\epsilon_j{}^2+1,1)\}_{j=1}^2\right\}_1^N \\ (1;\{1\}_1^N),(1;\{1\}_1^N):\left\{\{\psi_{rj}\}_{j=1}^2\right\}_1^N \end{matrix} \right) \end{aligned} \tag{36}$$

where $\psi_{rj} = \{(\epsilon_j{}^2, 1), (\alpha_{1,j}, 1), (\beta_{1,j}, 1), (\alpha_{2,j}, 1), (\beta_{2,j}, 1)\}$, $\nu_{ri,j} = \nu_{fi,j}\nu_{bi,j}$, and $\rho_{ri,j} = \rho_{fi,j}\rho_{bi,j}$. For IM/DD,

$$\gamma_{RIS} = \left(\frac{K}{w} \right)^2 H_{RIS}^2 \bar{\gamma}_{RIS} \tag{37}$$

After RV transformation, the PDF of γ_{RIS} is derived to be Eq. (38) (see Box I). Initially, it may appear that the SNR expression is solely derived based on the channel characteristics, independent of the noise variance. However, a closer examination reveals that this is not the case, as $\bar{\gamma}_{\mathrm{RIS}}$ can be expressed in terms of σ_n^2 as:

$$\bar{\gamma}_{\mathrm{RIS}} = \frac{R^2 P_s^2}{\sigma_n^2} \tag{39}$$

The CDF of the end-to-end SNR, denoted as $F_{\gamma_{RIS}}(\gamma_{RIS})$, is computed from its PDF as follows:

$$F_{\gamma}(\gamma) = \int_0^{\gamma} f_{\gamma}(x) dx \tag{40}$$

Substituting Eq. (38) into Eq. (40) and expanding N-MFHF in terms of Mellin–Barnes integrals to obtain:

$$\begin{aligned} F_{\gamma_{RIS}}(\gamma_{RIS}) = & \frac{\prod_{i=1}^{N} \prod_{j=1}^{2} \nu_{ri,j}}{2h_{lRIS}} \times \left(\frac{1}{2\pi\chi} \right)^N \times \prod_{i=1}^{N} \int_0^{\gamma_{RIS}} \int_{\mathcal{L}_i} \\ & \frac{\gamma_{RIS}^{-1}}{h_{l,RIS}\left(\Gamma(\sum_{i=1}^{N} \zeta_i) \right)^2} \times \prod_{i=1}^{N} \left\{ \frac{\prod_{j=1}^{2} A_{j,i}}{\prod_{j=1}^{2} \Gamma(\epsilon_j{}^2 + 1 - \zeta_i)} \right. \\ & \left. \left(\frac{w}{K} \prod_{j=1}^{2} \rho_{ri,j} \times \sqrt{\frac{\gamma_{RIS}}{\bar{\gamma}_{RIS}}} \right)^{\zeta_i} \right\} d\zeta_i d\gamma_{RIS} \end{aligned} \tag{41}$$

where $\chi = \sqrt{-1}$ is the imaginary unit, and $A_{j,i} = [\Gamma(\epsilon_j{}^2 - \zeta_i)\Gamma(\alpha_{1,j} - \zeta_i)\Gamma(\beta_{1,j} - \zeta_i)\Gamma(\alpha_{2,j} - \zeta_i)\Gamma(\beta_{2,j} - \zeta_i)[\Gamma(\zeta_i)]^2]$. Solving the inner integral in Eq. (41), we get

$$\int_0^{\gamma_{RIS}} \gamma_{RIS}{}^{-1+\sum_{i=1}^{N} \zeta_i} d\gamma_{RIS} = 2 \times \gamma_{RIS}{}^{\frac{1}{2}\sum_{i=1}^{N} \zeta_i} \frac{\Gamma(\sum_{i=1}^{N} \zeta_i)}{\Gamma(1 + \sum_{i=1}^{N} \zeta_i)} \tag{42}$$

Substituting Eq. (42) into Eq. (40) and employing the N-MFHF definition ([30], A.1), we obtain Eq. (43) (see Box II).

$$f_{\gamma_{RIS}}(\gamma_{RIS}) = \frac{\prod_{i=1}^{N}\prod_{j=1}^{2} \nu_{ri,j}}{2\gamma_{RIS}} \times H_{0,2:4,10;\ldots;4,10}^{0,0:10,2;\ldots;10,2}\left(\left\{ \frac{w}{K} \frac{\prod_{j=1}^{2} \rho_{rj}}{h_{lRIS}} \sqrt{\frac{\gamma_{RIS}}{\bar{\gamma}_{RIS}}} \right\}_1^N \middle| \begin{matrix} -:\left\{(1,1),(1,1),\{(\epsilon_j{}^2+1,1)\}_{j=1}^2\right\}_1^N \\ (1;\{1\}_1^N),(1;\{1\}_1^N):\left\{\{\psi_{r,j}\}_{j=1}^2\right\}_1^N \end{matrix} \right) \tag{38}$$

Box I.

$$F_{\gamma_{RIS}}(\gamma_{RIS}) = \prod_{i=1}^{N}\prod_{j=1}^{2} \nu_{ri,j} \times H_{0,2:4,10;\ldots;4,10}^{0,0:10,2;\ldots;10,2}\left(\left\{ \frac{w}{K} \frac{\prod_{j=1}^{2} \rho_{rj}}{h_{lRIS}} \sqrt{\frac{\gamma_{RIS}}{\bar{\gamma}_{RIS}}} \right\}_1^N \middle| \begin{matrix} -:\left\{(1,1),(1,1),\{(\epsilon_j{}^2+1,1)\}_{j=1}^2\right\}_1^N \\ (1;\{1\}_1^N),(0;\{1\}_1^N):\left\{\{\psi_{r,j}\}_{j=1}^2\right\}_1^N \end{matrix} \right) \tag{43}$$

Box II.

4. BER performance analysis

In this section, we derive mathematical expressions for the average BER of the LQAM-MPPM modulation scheme over the RIS-assisted MRR-UOWC channels. The BER of the LQAM-MPPM technique is the average of the BERs of both LQAM and MPPM techniques and is given as [32]:

$$\begin{aligned} \mathrm{BER}_{L\text{QAM-MPPM}} &= \frac{\log_2\binom{K}{w}}{\log_2\binom{K}{w}+wm}\mathrm{BER}_{\mathrm{MPPM}} \\ &+\frac{wm}{\log_2\binom{K}{w}+wm}\left[\mathrm{BER}_{L\text{QAM}}\left(1-\mathrm{SER}_{\mathrm{MPPM}}\right)+\frac{\mathrm{SER}_{\mathrm{MPPM}}}{2}\right] \end{aligned} \tag{44}$$

where $\mathrm{BER}_{L\text{QAM}}$L is the bit-error rate of traditional LQAM scheme, and $\mathrm{SER}_{\mathrm{MPPM}}$ and $\mathrm{BER}_{\mathrm{MPPM}}$ are the symbol-error rate and bit-error rate of the traditional MPPM scheme, respectively, which are related by

$$\mathrm{BER}_{\mathrm{MPPM}} \leq \frac{2^{\lfloor \log_2\binom{K}{w}\rfloor-1}}{2^{\lfloor \log_2\binom{K}{w}\rfloor}-1}\mathrm{SER}_{\mathrm{MPPM}} \tag{45}$$

The first term in Eq. (44) corresponds to the BER associated with the group of $\lfloor \log_2\binom{K}{w}\rfloor$ bits transmitted through MPPM. The second term represents the BER of the remaining wm bits, consisting of two segments. The first segment accounts for scenarios where the MPPM signal-slots are decoded correctly, while the second segment addresses cases where the MPPM signal-slots are decoded incorrectly. The next subsections are devoted to deriving UB expressions (Section 4.1) and approximate UB (Section 4.2) expressions for both $\mathrm{SER}_{\mathrm{MPPM}}$ and $\mathrm{BER}_{L\text{QAM}}$L in order to assess the BER of LQAM-MPPM technique using Eq. (44).

4.1. Upper-bound BER expressions

In this subsection, we perform comprehensive mathematical manipulations to derive a closed-form UB expression for the average BER of the LQAM-MPPM scheme in terms of the MFHF. Employing ([27], Eq.(07.34.26.0008.01)), the $\mathrm{SER}_{\mathrm{MPPM}}$ can be written as [33]:

$$\mathrm{SER}_{\mathrm{MPPM}}(\gamma_{RIS}) \leq \frac{\binom{K}{w}-1}{2\sqrt{\pi}} H_{1,2}^{2,0}\left(\phi_{\mathrm{s}}\gamma_{RIS}\middle|\begin{matrix}(1,1)\\(0,1),(0.5,1)\end{matrix}\right) \tag{46}$$

where $\phi_{\mathrm{s}} = \log_2\binom{K}{w}/\{4K\}$. The average SER is computed by taking the average of $\mathrm{SER}_{\mathrm{MPPM}}(\gamma_{RIS})$ from Eq. (46) across the pdf in Eq. (38) with respect to γ_{RIS}. Thus, the average $\mathrm{SER}_{\mathrm{MPPM}}$ is obtained by:

$$\mathrm{SER}_{\mathrm{MPPM}} = \int_0^{\infty} \mathrm{SER}_{\mathrm{MPPM}}(\gamma_{RIS}) f_{\gamma_{RIS}}(\gamma_{RIS}) \mathrm{d}\gamma_{RIS} \tag{47}$$

Substituting Eq. (46) into Eq. (38) and expanding N-MFHF in terms of Mellin–Barnes integrals to obtain:

$$\begin{aligned} \mathrm{SER}_{\mathrm{MPPM}} &\leq \frac{\binom{K}{w}-1}{4\sqrt{\pi}} \times \left(\frac{1}{2\pi\chi}\right)^{N+1} \times \prod_{i=1}^{N}\prod_{j=1}^{2} \nu_{ri,j} \\ &\times \prod_{i=1}^{N} \int_0^{\infty}\int_{\mathcal{L}}\int_{\mathcal{L}_i} \frac{\gamma_{RIS}^{-1}}{\left(\Gamma(\sum_{i=1}^{N}\zeta_i)\right)^2} \times \frac{\Gamma(-\zeta)\Gamma(0.5-\zeta)}{\Gamma(1-\zeta)} \\ &\times \left(\phi_{\mathrm{s}}\gamma_{RIS}\right)^{\zeta} \times \prod_{i=1}^{N}\left\{ \frac{\prod_{j=1}^{2} A_{j,i}}{\prod_{j=1}^{2}\Gamma(\epsilon_j{}^2+1-\zeta_i)} \right. \\ &\times \left. \left(\frac{w}{K}\frac{\prod_{j=1}^{2}\rho_{ri,j}}{h_{lRIS}} \times \sqrt{\frac{\gamma_{RIS}}{\bar{\gamma}_{RIS}}}\right)^{\zeta_i} \right\} d\zeta d\zeta_i d\gamma_{RIS} \end{aligned} \tag{48}$$

Applying the final value theorem to solve the inner integral in Eq. (48), we obtain:

$$\int_0^{\infty} \gamma_{RIS}{}^{\zeta-1+\frac{1}{2}\sum_{i=1}^{N}\zeta_i} d\gamma_{RIS} = \left(\frac{1}{\delta}\right)^{\zeta+\frac{1}{2}\sum_{i=1}^{N}\zeta_i} \Gamma\left(r+\frac{1}{2}\sum_{i=1}^{N}\zeta_i\right) \tag{49}$$

where δ is in the order 10^{-6}. Substituting Eq. (49) into Eq. (48) and employing the N-MFHF definition ([30], A.1), we obtain Eq. (50) (see Box III). The $\mathrm{BER}_{L\text{QAM}}$L can be written as [34]:

$$\begin{aligned} \mathrm{BER}_{L\text{QAM}}(\gamma_{RIS}) &= \frac{2}{m\sqrt{\pi}} \\ &\times \begin{cases} \frac{\sqrt{L}-1}{\sqrt{L}} \times H_{2,0}^{1,2}\left(\phi_{\mathrm{e}}\gamma_{RIS}\middle|\begin{matrix}(1,1)\\(0,1),(0.5,1)\end{matrix}\right); & \text{for even } m, \\ H_{2,0}^{1,2}\left(\phi_{\mathrm{o}}\gamma_{RIS}\middle|\begin{matrix}(1,1)\\(0,1),(0.5,1)\end{matrix}\right); & \text{for odd } m. \end{cases} \end{aligned} \tag{51}$$

where $\phi_{\mathrm{e}} = \sum_{n=1}^{\sqrt{L}/2}(2n-1)^2 \times 3M^2/\{4(L-1)\}$, $\phi_{\mathrm{o}} = 3M^2/\{4(L-1)\}$, and M is the modulation-index. The average BER is obtained by averaging of $\mathrm{BER}_{L\text{QAM}}\mathrm{L}(\gamma_{RIS})$ in Eq. (51) over the pdf in Eq. (38) with respect to γ_{RIS}. Thus, the average $\mathrm{BER}_{L\text{QAM}}$L is obtained by:

$$\mathrm{BER}_{L\text{QAM}} = \int_0^{\infty} \mathrm{BER}_{L\text{QAM}}(\gamma_{RIS}) f_{\gamma_{RIS}}(\gamma_{RIS}) d\gamma_{RIS} \tag{52}$$

In a manner similar to the derivation of Eq. (50), we obtain Eq. (53) (see Box IV) for $\mathrm{BER}_{L\text{QAM}}$L. Finally, the UB expression for the average BER of LQAM-MPPM is derived by replacing Eqs. (50), (45), and (53) in Eq. (44).

4.2. Approximate upper-bound BER expressions

To assess the accuracy of the expressions derived in the preceding subsection, we will derive approximate expressions using GLQR. First, we express the average of $\mathrm{SER}_{\mathrm{MPPM}}(\gamma_{RIS})$ as follows [35]:

$$\mathrm{SER}_{\mathrm{MPPM}} = -\int_0^{\infty} \frac{\mathrm{dSER}_{\mathrm{MPPM}}(\gamma_{RIS})}{\mathrm{d}\gamma_{RIS}} F_{\gamma_{RIS}}(\gamma_{RIS}) \mathrm{d}\gamma_{RIS} \tag{54}$$

$$\mathrm{SER}_{\mathrm{MPPM}}^{\mathrm{exact}} \leq \frac{\binom{K}{w}-1}{4\sqrt{\pi}} \times \prod_{i=1}^{N}\prod_{j=1}^{2} \nu_{ri,j} \times H_{1,3:4,10;\ldots;4,10;1,2}^{0,1:10,2;\ldots;10,2;2,0}\left(\left\{ \frac{w}{K} \frac{\prod_{j=1}^{2}\rho_{rj}}{h_{lRIS}\sqrt{\delta\overline{\gamma}_{RIS}}} \right\}_1^N, \frac{\phi_s}{\delta} \middle| \begin{matrix} (1;\{0.5\}_1^N,1):(1,1),\left\{(1,1),(1,1),\{(\epsilon_j{}^2+1,1)\}_{j=1}^2\right\}_1^N \\ (1;\{1\}_1^N,0),(1;\{1\}_1^N,0),(1;\{0.5\}_1^N,0.5):\left\{\{\psi_{rj}\}_{j=1}^2\right\}_1^N \end{matrix} \right) \tag{50}$$

Box III.

$$\mathrm{BER}_{LQAM}^{\mathrm{exact}} = \frac{\prod_{i=1}^{N}\prod_{j=1}^{2}\nu_{ri,j}}{m\sqrt{\pi}} \times \begin{cases} \frac{\sqrt{L}-1}{\sqrt{L}} \times H_{1,3:4,10;\ldots;4,10;1,2}^{0,1:10,2;\ldots;10,2;2,0}\left(\left\{ \frac{w}{K} \frac{\prod_{j=1}^{2}\rho_{rj}}{h_{lRIS}\sqrt{\delta\overline{\gamma}_{RIS}}} \right\}_1^N, \frac{\phi_e}{\delta} \middle| \begin{matrix} (1;\{0.5\}_1^N,1):(1,1),\left\{(1,1),(1,1),\{(\epsilon_j{}^2+1,1)\}_{j=1}^2\right\}_1^N \\ (1;\{1\}_1^N,0),(1;\{1\}_1^N,0),(1;\{0.5\}_1^N,0.5):\left\{\{\psi_{rj}\}_{j=1}^2\right\}_1^N \end{matrix} \right); \text{for even } m, \\ H_{1,3:4,10;\ldots;4,10;1,2}^{0,1:10,2;\ldots;10,2;2,0}\left(\left\{ \frac{w}{K} \frac{\prod_{j=1}^{2}\rho_{rj}}{h_{lRIS}\sqrt{\delta\overline{\gamma}_{RIS}}} \right\}_1^N, \frac{\phi_o}{\delta} \middle| \begin{matrix} (1;\{0.5\}_1^N,1):(1,1),\left\{(1,1),(1,1),\{(\epsilon_j{}^2+1,1)\}_{j=1}^2\right\}_1^N \\ (1;\{1\}_1^N,0),(1;\{1\}_1^N,0),(1;\{0.5\}_1^N,0.5):\left\{\{\psi_{rj}\}_{j=1}^2\right\}_1^N \end{matrix} \right); \text{for odd } m. \end{cases} \tag{53}$$

Box IV.

$$\mathrm{SER}_{\mathrm{MPPM}}^{\mathrm{approx.}} \leq \frac{\binom{K}{w}-1}{2\sqrt{\pi}} \prod_{i=1}^{N}\prod_{j=1}^{2}\nu_{ri,j} \times \sum_{a=1}^{q}\frac{s_a}{\sqrt{u_a}} \times H_{0,2:4,10;\ldots;4,10}^{0,0:10,2;\ldots;10,2}\left(\left\{ \frac{w}{K} \frac{\prod_{j=1}^{2}\rho_{rj}}{h_{lRIS}} \sqrt{\frac{z_a}{\phi_s\overline{\gamma}_{RIS}}} \right\}_1^N \middle| \begin{matrix} -:\left\{(1,1),(1,1),\{(\epsilon_j{}^2+1,1)\}_{j=1}^2\right\}_1^N \\ (1;\{1\}_1^N),(0;\{1\}_1^N):\left\{\{\psi_{r,j}\}_{j=1}^2\right\}_1^N \end{matrix} \right) \tag{58}$$

Box V.

$$\mathrm{BER}_{LQAM}^{\mathrm{approx.}} = \frac{\prod_{i=1}^{N}\prod_{j=1}^{2}\nu_{ri,j}}{m\sqrt{\pi}} \times \sum_{a=1}^{q}\frac{s_a}{\sqrt{u_a}} \times \begin{cases} \frac{\sqrt{L}-1}{\sqrt{L}} \times H_{0,2:4,10;\ldots;4,10}^{0,0:10,2;\ldots;10,2}\left(\left\{ \frac{w}{K} \frac{\prod_{j=1}^{2}\rho_{rj}}{h_{lRIS}} \sqrt{\frac{z_a}{\phi_e\overline{\gamma}_{RIS}}} \right\}_1^N \middle| \begin{matrix} -:\left\{(1,1),(1,1),\{(\epsilon_j{}^2+1,1)\}_{j=1}^2\right\}_1^N \\ (1;\{1\}_1^N),(0;\{1\}_1^N):\left\{\{\psi_{r,j}\}_{j=1}^2\right\}_1^N \end{matrix} \right); \text{for even } m, \\ H_{0,2:4,10;\ldots;4,10}^{0,0:10,2;\ldots;10,2}\left(\left\{ \frac{w}{K} \frac{\prod_{j=1}^{2}\rho_{rj}}{h_{lRIS}} \sqrt{\frac{z_a}{\phi_o\overline{\gamma}_{RIS}}} \right\}_1^N \middle| \begin{matrix} -:\left\{(1,1),(1,1),\{(\epsilon_j{}^2+1,1)\}_{j=1}^2\right\}_1^N \\ (1;\{1\}_1^N),(0;\{1\}_1^N):\left\{\{\psi_{r,j}\}_{j=1}^2\right\}_1^N \end{matrix} \right); \text{for odd } m. \end{cases} \tag{59}$$

Box VI.

Substituting from Eqs. (46), (43) in Eq. (54) leads to

$$\mathrm{SER}_{\mathrm{MPPM}} \leq -\int_0^{\infty} \frac{\binom{K}{w}-1}{2\sqrt{\pi}} \prod_{i=1}^{N}\prod_{j=1}^{2}\nu_{ri,j} \times \exp\left(-\phi_s\gamma_{RIS}\right) \times H_{0,2:4,10;\ldots;4,10}^{0,0:10,2;\ldots;10,2}\left(\left\{ \frac{w}{K} \frac{\prod_{j=1}^{2}\rho_{rj}}{h_{lRIS}} \sqrt{\frac{\gamma_{RIS}}{\overline{\gamma}_{RIS}}} \right\}_1^N \middle| \begin{matrix} -:\left\{(1,1),(1,1),\{(\epsilon_j{}^2+1,1)\}_{j=1}^2\right\}_1^N \\ (1;\{1\}_1^N),(0;\{1\}_1^N):\left\{\{\psi_{r,j}\}_{j=1}^2\right\}_1^N \end{matrix} \right) \times \sqrt{\phi_s} \times {\gamma_{RIS}}^{-1/2} \mathrm{d}\gamma_{RIS} \tag{55}$$

By performing change of variable $z = \phi_s\gamma_{RIS}$, Eq. (55) can be rewritten as:

$$\mathrm{SER}_{\mathrm{MPPM}} \leq \int_0^{\infty} \frac{\binom{K}{w}-1}{2\sqrt{\pi}} \prod_{i=1}^{N}\prod_{j=1}^{2}\nu_{ri,j} \exp(-z) \times z^{-1/2} \times H_{0,2:4,10;\ldots;4,10}^{0,0:10,2;\ldots;10,2}\left(\left\{ \frac{w}{K} \frac{\prod_{j=1}^{2}\rho_{rj}}{h_{lRIS}} \sqrt{\frac{z}{\overline{\gamma}_{RIS}\phi_s}} \right\}_1^N \middle| \begin{matrix} -:\left\{(1,1),(1,1),\{(\epsilon_j{}^2+1,1)\}_{j=1}^2\right\}_1^N \\ (1;\{1\}_1^N),(0;\{1\}_1^N):\left\{\{\psi_{r,j}\}_{j=1}^2\right\}_1^N \end{matrix} \right) \mathrm{d}z \tag{56}$$

Using generalized GLQR given by [36]:

$$\int_0^{\infty} e^{-u} f(u) du = \sum_{a=1}^{q} s_a f(u_a) \tag{57}$$

where $q > 1$ represents the number of terms, and for any $a \in \{1, 2, \ldots, q\}$, u_a is the ath root of Laguerre polynomial $L_q(X)$ with degree q, and s_a is the corresponding weighting coefficient, to obtain Eq. (58) (see Box V). In a manner similar to the derivation of Eq. (58), we obtain Eq. (59) (see Box VI) for BER_{LQAM}. Finally, the UB expression for the average BER of LQAM-MPPM is derived by replacing Eqs. (58), (45), and (59) in Eq. (44).

5. Results and discussion

In this section, the analytical average BER of an LQAM-MPPM RIS-assisted MRR-UOWC system is investigated. The system adopts IM/DD and the channel is characterized by path loss, G–G turbulence, and PE over both clear ocean and coastal ocean environments. The derived expressions from previous sections are utilized, and the MFHF implementation in MATLAB code [37] is employed to evaluate these expressions.

The assumed configuration places the optical RIS midway between the transceiver and the MRR unit, with the distance between the transceiver and the RIS module being equal to the distance between the RIS module and the MRR unit, both set to 5 m. The utilized system parameters are: $\lambda = 532$ nm, $M = 0.8$, $T_s = 10^{-9}$s, $R = 0.5$ A/W, $\eta = 0.8$, $A = 50\,\mathrm{cm}^2$, $R_L = 50\,\Omega$, RIN $= -130$ dB/Hz, $\alpha_{1,1} = 3.7258$, $\beta_{1,1} = 3$, $\alpha_{2,1} = 3.5216$, $\beta_{2,1} = 1.5$, $\alpha_{1,2} = 3.4642$, $\beta_{1,2} = 2$, $\alpha_{2,2} = 3.2245$, $\beta_{2,2} = 1.2$, $A_o = 1$, $\epsilon_1 = 1.3$, and $\epsilon_2 = 1.1$. In the case of clear ocean, $c(\lambda) = 0.1514$, m^{-1}, and for the coastal ocean, it is 0.399 m^{-1}.

As shown in Fig. 4, we investigate the performance of the considered RIS-assisted MRR-UOWC system by plotting average BER of the LQAM-MPPM technique for three scenarios: (a) with $N = 5$, (b) with $N = 10$, and (c) with $N = 15$. Fig. 4 illustrates how the average BER of

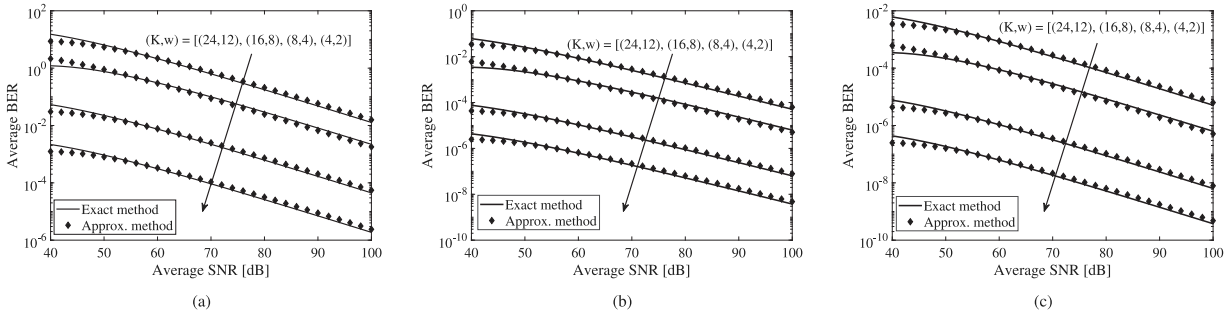

Fig. 4. Average BER for an RIS-assisted MRR-UOWC system in clear ocean adopting 4QAM-MPPM with (K, w, R_b) = (4, 2, 1.5 Gbps), (8, 4, 1.75 Gbps), (16, 8, 1.8125 Gbps), (24, 12, 2.625 Gbps) versus average SNR in dB for three scenarios: (a) with N = 5, (b) with N = 10, and (c) with N = 15.

the hybrid technique is influenced by the cardinality of the MPPM constellation.

Furthermore, Fig. 4(a)–4(c) illustrate the enhancement in the performance of an RIS-assisted MRR-UOWC system as the number of RIS elements increases and depict the average SNR required to achieve specific average BER levels. As illustrated in the figures, the cardinality exhibits a direct proportionality with the average BER since an increase in the number of MPPM symbols results in a higher SER for MPPM, consequently leading to an elevated average BER for the LQAM-MPPM. This is due to several factors. The complexity of the modulation scheme increases with higher cardinality, demanding more power for signal transmission and potentially compromising modulation efficiency. This intricate modulation process, coupled with higher cardinality, imposes computational burdens on both the transmitter and receiver, leading to possible delays. Moreover, higher cardinality introduces challenges in receiver design, causing increased hardware complexity and costs. The heightened complexity contributes to difficulties in accurate symbol identification, raising the likelihood of errors during the demodulation process. The system becomes more sensitive to noise and interference, impacting its ability to distinguish symbols and increasing the probability of reception errors. Additionally, higher cardinality may result in increased system latency and limitations in benefiting from diversity gain in fading channels, affecting overall reliability. In scenarios with low SNR, higher cardinality increases challenges in accurate symbol detection, leading to a higher rate of decoding errors. Achieving a balance between increasing cardinality and maintaining manageable system complexity is crucial for optimal communication performance, making moderate cardinality values a preferred choice in some cases to strike a balance between system complexity and performance improvement. Furthermore, the cardinality demonstrates a direct proportionality to the attained data rate. Therefore, an increment in the cardinality of the MPPM constellation results in an increase in average BER (indicative of reduced system performance) while simultaneously enhancing the maximum achievable data rate.

As depicted in Fig. 4(a) with N = 5, the LQAM-MPPM exhibits a significant degradation in average BER performance, dropping to approximately 10^0 at an average SNR of 70 dB. This is observed for an MPPM constellation with cardinality (K, w) = (24,12), achieving a data rate of 2.625 Gbps. Moreover, a reduction in the cardinality results in a decrease in average BER (indicating improved system performance) and a simultaneous increase in the maximum achievable data rate. For (K, w) = (16,8), the average BER decreases to around 10^{-1} at an average SNR of 70 dB, achieving a data rate of 1.8125 Gbps. Likewise, with (K, w) = (8,4), the average BER decreases to below 10^{-2} at an average SNR of 70 dB, yielding a data rate of 1.75 Gbps. Finally, for (K, w) = (4,2), the average BER diminishes to approximately 10^{-4} at an average SNR of 70 dB, with a corresponding data rate of 1.5 Gbps.

The average BER performance exhibits a significant enhancement with an increase in the number of RIS elements. Increasing the number of RIS elements leads to a reduction in average BER (indicating improved system performance). In Fig. 4(b), with N = 10, the LQAM-MPPM experiences a significant degradation in average BER, reaching around 10^{-2} at an average SNR of 70 dB, given an MPPM constellation cardinality of (K, w) = (24,12). Moreover, diminishing the cardinality results in a decrease in average BER, further enhancing system performance. For (K, w) = (16,8), the average BER drops to approximately 10^{-3} at an average SNR of 70 dB, while for (K, w) = (8,4), the average BER decreases to around 10^{-5} at the same average SNR. In the case of (K, w) = (4,2), the average BER diminishes to below 10^{-6} at an average SNR of 70 dB.

Similarly, in Fig. 4(c) with N = 15, an increase in N indicates improved system performance. Additionally, the average BER performance for the LQAM-MPPM is significantly degraded to around 10^{-3} at an average SNR of 70 dB with the MPPM constellation cardinality being (K, w) = (24,12). Again, reducing the cardinality results in decreased average BER, indicating enhanced system performance. For (K, w) = (16,8), the average BER decreases to below 10^{-4} at an average SNR of 70 dB, and for (K, w) = (8,4), the average BER drops to around 10^{-6} at the same average SNR. Finally, for (K, w) = (4,2), the average BER decreases to below 10^{-7} at an average SNR of 70 dB. Fig. 4 shows a significant level of agreement between UB and approximate UB expressions with q = 100.

As illustrated in Fig. 5, with a fixed value of N, the hybrid technique featuring (K, w, L, R_b) = (12, 2, 4, 833 Mbps) demonstrates superior performance compared to the MPPM technique with (K, w, R_b) = (12, 5, 750 Mbps) as the average SNR increases. This performance advantage is evident across three scenarios: (a) N = 5, (b) N = 10, and (c) N = 15. Specifically, using the hybrid technique, the system outperforms MPPM by approximately 8 dB at an average BER of 10^{-4} in clear ocean conditions. Moreover, in coastal ocean conditions with comparable data rates, the system employing the hybrid technique exhibits a lower average BER floor compared to that of MPPM.

In Fig. 5(a) for clear ocean and N = 5, the system achieves an average BER of 10^{-4} at approximately 78 dB and 87 dB for LQAM-MPPM and MPPM techniques, respectively. Conversely, in coastal ocean conditions and for N = 5, the system achieves an average BER of 10^{-4} at around 95 dB and 104 dB for LQAM-MPPM and MPPM techniques, respectively. In Fig. 5(b) for clear ocean and N = 10, the system attains an average BER of 10^{-4} at about 68 dB and 75 dB for LQAM-MPPM and MPPM techniques, respectively. Similarly, in coastal ocean conditions and for N = 10, the system achieves an average BER of 10^{-4} at approximately 84 dB and 91 dB for LQAM-MPPM and MPPM techniques, respectively. In Fig. 5(c) for clear ocean and N = 15, the system achieves an average BER of 10^{-4} at around 52 dB and 60 dB for LQAM-MPPM and MPPM techniques, respectively. Conversely, in coastal ocean conditions and for N = 15, the system attains an average BER of 10^{-4} at approximately 65 dB and 73 dB for LQAM-MPPM and MPPM techniques, respectively. Similar to Fig. 4, this figure shows a significant level of agreement between UB and approximate UB expressions with q = 100.

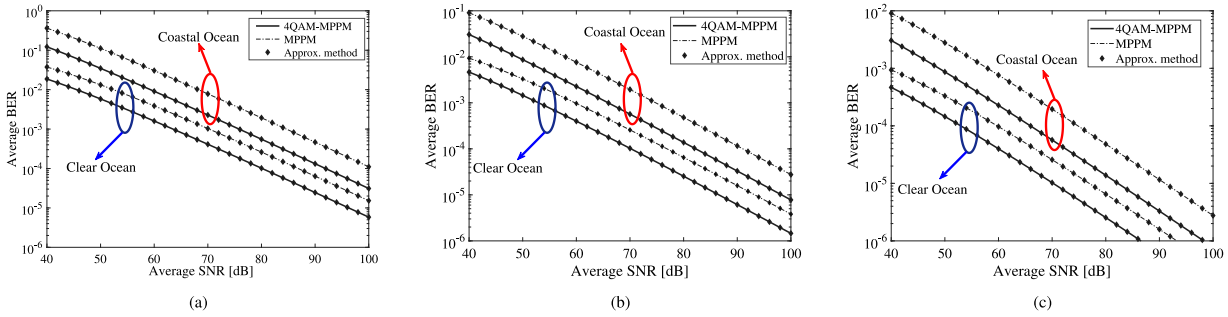

Fig. 5. Average BER for an RIS-assisted MRR-UOWC system adopting both LQAM-MPPM with (K, w, L, R_b) = (12, 2, 4, 833 Mbps) and MPPM with (K, w, R_b) = (12, 5, 750 Mbps) versus average SNR in dB for three scenarios: (a) with N = 5, (b) with N = 10, and (c) with N = 15.

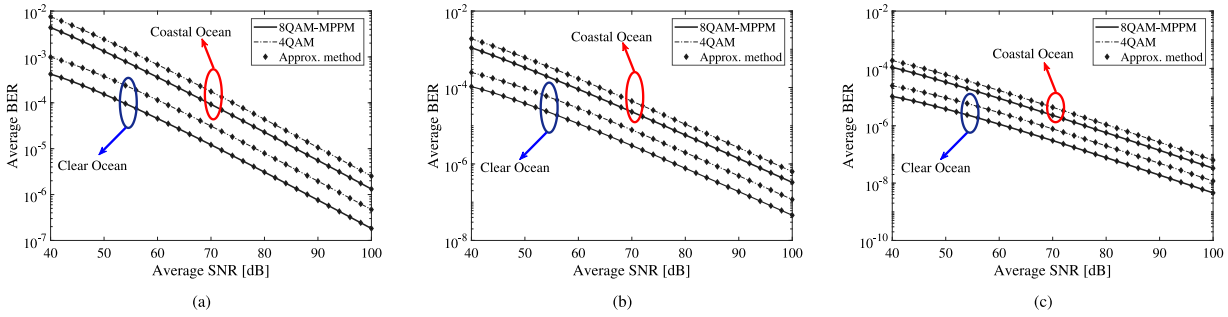

Fig. 6. Average BER for an RIS-assisted MRR-UOWC system adopting both LQAM-MPPM with (K, w, L, R_b) = (4, 2, 8, 2 Gbps) and LQAM with (L, R_b) = (4, 2 Gbps) versus average SNR in dB for three scenarios: (a) with N = 5, (b) with N = 10, and (c) with N = 15.

As depicted in Fig. 6, with a fixed value of N, the hybrid technique featuring (K, w, L, R_b) = (4, 2, 8, 2 Gbps) consistently outperforms the LQAM technique with (L, R_b) = (4, 2 Gbps) as the average SNR increases. This superiority is observed across three scenarios: (a) N = 5, (b) N = 10, and (c) N = 15. Specifically, with the hybrid technique, the system outperforms LQAM by approximately 6 dB at an average BER of 10^{-4} in clear ocean conditions. Furthermore, under comparable data rates, the system employing the hybrid technique exhibits a lower average BER floor compared to that of LQAM in coastal ocean conditions.

In Fig. 6(a) for clear ocean and N = 5, the system achieves an average BER of 10^{-4} at approximately 51 dB and 57 dB for LQAM-MPPM and LQAM techniques, respectively. Conversely, in coastal ocean conditions and for N = 5, the system achieves an average BER of 10^{-4} at around 66 dB and 72 dB for LQAM-MPPM and LQAM techniques, respectively. In Fig. 6(b) for clear ocean and N = 10, the system attains an average BER of 10^{-4} at about 40 dB and 46 dB for LQAM-MPPM and LQAM techniques, respectively. Similarly, in coastal ocean conditions and for N = 10, the system achieves an average BER of 10^{-4} at approximately 60 dB and 66 dB for LQAM-MPPM and LQAM techniques, respectively. In Fig. 6(c) for clear ocean and N = 15, the system achieves an average BER of 10^{-4} at around 32 dB and 38 dB for LQAM-MPPM and LQAM techniques, respectively. Conversely, in coastal ocean conditions and for N = 15, the system attains an average BER of 10^{-4} at approximately 40 dB and 44 dB for LQAM-MPPM and LQAM techniques, respectively. Similar to Fig. 6, this figure shows a significant level of agreement between UB and approximate UB expressions with q = 100.

6. Conclusions

This paper focuses on the integration of RIS in MRR-UOWC systems and explores its impact on system performance, offering valuable insights into the behavior of such systems. The study investigates how the cardinality of the MPPM constellation affects both the data rate and average BER in an IM/DD RIS-assisted MRR-UOWC system using the spectral-power-efficient LQAM-MPPM technique.

In scenarios with comparable data rates, our results demonstrate that the average BER performance of the analyzed system, employing the LQAM-MPPM technique, outperforms that of systems utilizing traditional LQAM and MPPM techniques, while achieving higher power efficiency. The results highlight the substantial influence of the number of RIS elements on overall system performance, indicating that an increase in the number of RIS elements results in reduced transmitted power requirements to achieve a lower average BER. This is observed for both the hybrid technique and conventional techniques across various water types, with the hybrid technique demonstrating superior performance.

Additionally, the results indicate that, within the considered composite channel models, clear ocean conditions outperform coastal ocean conditions. Achieving optimal performance is crucial for the success of UOWC applications, and our study underscores the importance of incorporating RIS in UOWC systems. We propose that relying solely on DT channel studies may not cover all underwater scenarios. Considering realistic non-line-of-sight behavior in the underwater channel and examining the RIS-assisted MRR-UOWC system would yield significant implications.

CRediT authorship contribution statement

Amr G. AbdElKader: Writing – original draft, Methodology, Investigation, Conceptualization. **Ahmed Allam:** Writing – review & editing, Supervision, Conceptualization. **Kazutoshi Kato:** Writing – review & editing, Supervision. **Hossam M.H. Shalaby:** Writing – review & editing, Supervision, Conceptualization.

Declaration of competing interest

The authors declare that they have no known competing financial interests or personal relationships that could have appeared to influence the work reported in this paper.

Data availability

No data was used for the research described in the article.

Declaration of Generative AI and AI-assisted technologies in the writing process

This article did not apply any AI and AI-assisted technologies in the writing process.

Acknowledgment

This work is supported by the Ministry of Higher Education (MoHE), Egypt.

Funding

This research did not receive any specific grant from funding agencies in the public, commercial, or not-for-profit sectors.

References

[1] H. Kaushal, G. Kaddoum, Underwater optical wireless communication, IEEE access 4 (2016) 1518–1547.
[2] Z. Zeng, S. Fu, H. Zhang, Y. Dong, J. Cheng, A survey of underwater optical wireless communications, IEEE Commun. Surv. Tutor. 19 (2016) 204–238.
[3] P. Sajmath, R.V. Ravi, K.A. Majeed, Underwater wireless optical communication systems: a survey, in: 2020 7th international conference on smart structures and systems, ICSSS, IEEE, 2020, pp. 1–7.
[4] M.A. ElMossallamy, H. Zhang, L. Song, K.G. Seddik, Z. Han, G.Y. Li, Reconfigurable intelligent surfaces for wireless communications: Principles, challenges, and opportunities, IEEE Trans. Cogn. Commun. Netw. 6 (2020) 990–1002.
[5] T.-H. Ho, Pointing, Acquisition, and Tracking Systems for Free-Space Optical Communication Links, University of Maryland, College Park, 2007.
[6] C. Quintana, Q. Wang, D. Jakonis, O. Oberg, G. Erry, D. Platt, Y. Thueux, G. Faulkner, H. Chun, A. Gomez, et al., A high speed retro-reflective free space optics links with UAV, J. Lightwave Technol. 39 (2021) 5699–5705.
[7] G. Yang, C. Li, J. Li, H. Geng, M. Bi, B. Fan, T. Wang, Performance analysis of full duplex modulating retro-reflector free-space optical communications over single and double Gamma-Gamma fading channels, IEEE Trans. Commun. 66 (2018) 3597–3609.
[8] D. Selimis, K.P. Peppas, G.C. Alexandropoulos, F.I. Lazarakis, On the performance analysis of RIS-empowered communications over Nakagami-m fading, IEEE Commun. Lett. 25 (2021) 2191–2195.
[9] V. Jamali, H. Ajam, M. Najafi, B. Schmauss, R. Schober, H.V. Poor, Intelligent reflecting surface assisted free-space optical communications, IEEE Commun. Mag. 59 (2021) 57–63.
[10] I. Trigui, W. Ajib, W.-P. Zhu, A comprehensive study of reconfigurable intelligent surfaces in generalized fading, 2020, arXiv preprint arXiv:2004.02922.
[11] L. Yang, W. Guo, I.S. Ansari, Mixed dual-hop FSO-RF communication systems through reconfigurable intelligent surface, IEEE Commun. Lett. 24 (2020) 1558–1562.
[12] J. Wang, W. Zhang, X. Bao, T. Song, C. Pan, Outage analysis for intelligent reflecting surface assisted vehicular communication networks, in: GLOBECOM 2020-2020 IEEE Global Communications Conference, IEEE, 2020, pp. 1–6.
[13] L. Kong, J. He, Y. Ai, S. Chatzinotas, B. Ottersten, Channel modeling and analysis of reconfigurable intelligent surfaces assisted vehicular networks, in: 2021 IEEE International Conference on Communications Workshops, ICC Workshops, IEEE, 2021, pp. 1–6.
[14] V.K. Chapala, S.M. Zafaruddin, RIS-assisted multihop FSO/RF hybrid system for vehicular communications over generalized fading, 2021, arXiv preprint arXiv:2112.12944.
[15] G. Yang, J. Zhang, J. Zhang, M. Bi, T. Chen, S. You, X. Zhou, T. Wang, J. Li, H. Geng, Wavefront compensation with the micro corner-cube reflector array in modulating retroreflector free-space optical channels, J. Lightwave Technol. 39 (2020) 1355–1363.
[16] E. Rosenkrantz, S. Arnon, 1550 Nm modulating retroreflector based on coated nanoparticles for free-space optical communication, Appl. Opt. 54 (2015) 5309–5313.
[17] J. Yanmei, L. Congmin, S. Pengfei, L. Lu, Modulated retro-reflector-based physical-layer network coding for space optical communications, IEEE Access 9 (2021) 44868–44880.
[18] M.T. Dabiri, M. Rezaee, L. Mohammadi, F. Javaherian, V. Yazdanian, M.O. Hasna, M. Uysal, Modulating Retroreflector Based Free Space Optical Link for UAV-to-Ground Communications, IEEE Trans. Wireless Commun. 21 (2022) 8631–8645.
[19] H.S. Khallaf, H.M. Shalaby, Proposal of a hybrid QAM-MPPM technique for optical communications systems, in: 2014 16th International conference on transparent optical networks, ICTON, IEEE, 2014, pp. 1–4.
[20] H.M. Shalaby, Maximum achievable constrained power efficiencies of MPPM-LQAM techniques, IEEE Photonics Technol. Lett. 27 (2015) 1265–1268.
[21] A.G. AbdElKader, A. Allam, K. Kato, H.M. Shalaby, Performance enhancement of MRR underwater optical communications using LQAM-MPPM, in: 2022 Asia Communications and Photonics Conference, ACP, IEEE, 2022, pp. 473–476.
[22] H. Du, J. Zhang, J. Cheng, B. Ai, Millimeter wave communications with reconfigurable intelligent surfaces: Performance analysis and optimization, IEEE Trans. Commun. 69 (2021) 2752–2768.
[23] P.H. Mohamed, M.A. El-Shimy, H.M. Shalaby, H.N. Kheirallah, FSO channel modelling and performance evaluation over dust combined with gg atmospheric turbulence, NRSC, in: 2023 40th National Radio Science Conference, 1, IEEE, 2023, pp. 121–130.
[24] X. Luan, P. Yue, X. Yi, Scintillation index of an optical wave propagating through moderate-to-strong oceanic turbulence, J. Opt. Soc. Amer. A 36 (2019) 2048–2059.
[25] A.A. Farid, S. Hranilovic, Outage capacity optimization for free-space optical links with pointing errors, J. Lightwave Technol. 25 (2007) 1702–1710.
[26] K.-J. Jung, S.S. Nam, M.-S. Alouini, Y.-C. Ko, Unified finite series approximation of FSO performance over strong turbulence combined with various pointing error conditions, IEEE Trans. Commun. 68 (2020) 6413–6425.
[27] W. Research, The mathematical functions site, 1998, https://functions.wolfram.com. (Accessed: 09 Dec 2023).
[28] P.P. Phookan, S. Anees, Performance analysis of distributed alamouti based UWOC system, in: 2020 3rd International Conference on Advanced Communication Technologies and Networking, CommNet, IEEE, 2020, pp. 1–5.
[29] N. Hai, H. Srivastava, The convergence problem of certain multiple Mellin-Barnes contour integrals representing H-functions in several variables, Comput. Math. Appl. 29 (1995) 17–25.
[30] A.M. Mathai, R.K. Saxena, H.J. Haubold, The H-function: Theory and Applications, Springer Science & Business Media, 2009.
[31] P.H. Mohamed, M.A. El-Shimy, H.M. Shalaby, H.N. Kheirallah, Hybrid FSO/RF system over proposed random dust attenuation model based on real-time data combined with G–G atmospheric turbulence, Opt. Commun. 549 (2023) 129891.
[32] A.E.-R.A. El-Fikky, A.S. Ghazy, H.S. Khallaf, E.M. Mohamed, H.M. Shalaby, M.H. Aly, On the performance of adaptive hybrid MQAM–MPPM scheme over Nakagami and log-normal dynamic visible light communication channels, Appl. Opt. 59 (2020) 1896–1906.
[33] S.A. El-Meadawy, H.M. Shalaby, N.A. Ismail, F.E. Abd El-Samie, N.F. Soliman, A.D. Algarni, W. El-Shafai, A.E. Farghal, Proposal of hybrid NOAM-MPPM technique for Gamma-Gamma turbulence channel with pointing error and different deep learning techniques, IEEE Access 10 (2021) 10295–10309.
[34] K. Anbarasi, C. Hemanth, R. Sangeetha, Block error rate performance analysis of RS coded M-QAM modulated coherent OFDM-FSO system, Opt. Quantum Electron. 55 (2023) 78.
[35] A. Li, W. Wang, P. Wang, W. Pang, W. Chen, Y. Qin, SER performance investigation of a MPPM relay-aided FSO system with three decision thresholds over EW fading channel considering pointing errors, Opt. Commun. 487 (2021) 126803.
[36] C.S. Shetty, R.P. Naik, U.S. Acharya, W.-Y. Chung, Performance analysis of MIMO-EGC system for the underwater vertical wireless optical communication link, IEEE Access (2023).
[37] K.P. Peppas, A new formula for the average bit error probability of dual-hop amplify-and-forward relaying systems over generalized shadowed fading channels, IEEE Wirel. Commun. Lett. 1 (2012) 85–88.